CHAPTER II

LITERATURE REVIEWS

In this chapter, many aspects of star formation and bipolar outflows will be discussed, and the types of masers classified.

2.1 Star Formation

2.1.1 The Star Formation Process

The star formation process is an important and not fully understood problem in astrophysics. In the last few decades, great progress has been made in understanding this problem through observations at many wavelengths such as optical, infrared, centimetre and millimetre, and through theoretical models which attempt to explain the observed relationships between the clouds in which the stars are forming and the stellar properties (Shu et al., 1987; Shu, 1995; Lada, 1995; Shu et al., 2000).

The process of star formation can be divided into two cases dependent upon whether the stars are of high or low mass. The process of low-mass star formation is fairly well understood. The accepted model (Shu et al., 1987), which is supported by other theoretical and observational results (Evans 1999 and references therein), requires a disc and a young stellar object (YSO) outflow system. In fact, bipolar molecular outflows associated with low-mass stars are believed to be driven by jets which can be observed on sub-arcsecond scales. This constitutes the best evidence for collimation on the smallest scales yet known (Anglada, 1996). However, the process of high-mass star formation is not well understood. Low- and high-mass stars are distinguished from each other by the timescales over which they form: low mass stars form in a time short compared with the Kelvin-Helmholtz time, $t_{KH} = \frac{GM_r^2}{R_* L_*}$, where G is gravitational constant, M_r is the mass interior radius, R_* is the radius of the star and L_* is the luminosity of the star, whereas high-mass stars form in a time $\geq t_{KH}$. The division between low- and high-mass stars is considered to be at a mass of $8M_\odot$. Protostars that form stars with masses below this value have luminosities dominated by accretion, and they form from cores that have masses of the order of the thermal Jeans mass. Protostars above this mass have luminosities that are dominated by nuclear burning unless the accretion rate is very high, and if they form from molecular cores, those cores are significantly above the thermal Jeans mass (McKee and Ostriker, 2007).

2.1.1.1 Low-Mass Star Formation

Understanding the star-formation process in low-mass stars is important, not only in itself, but also because it has many factors in common with high-mass star formation. Star formation starts when gravity begins to dominate over heat, causing a cloud to lose its equilibrium and to contract. Only after the cloud

has undergone radical changes in its internal structure will equilibrium be finally restored. It has been well established that clouds must support themselves against their own gravitational forces or the star formation rate would be much larger than observed (Zuckerman et al. 1974). The observed average temperature of molecular clouds (10-20 K) implies that thermal pressure is unable to provide the necessary support except on the smallest size scales (Dickman and Clemens, 1983; Myers, 1983). Alternative supporting mechanisms for self gravitating interstellar clouds, such as magnetic fields, rotation and turbulence, have had to be invoked at one time or another.

Shu et al. (1987) concluded that the first stage of star formation is the formation of slowly rotating cloud cores (see Figure 2.1). In subcritical clumps this occurs through the slow leakage of magnetic (and turbulent) support by ambipolar diffusion; in supercritical clumps, the clump may also fragment as it contracts and flattens as a whole. As long as the core formation process occurs relatively slowly (i.e. with a time scale that is longer than the characteristic signal crossing time), the cores probably asymptotically approach centrally concentrated states that resemble singular isothermal spheres. However, such end states cannot actually be reached because they are unstable. The second stage begins when a condensing cloud core passes the brink of instability and collapses dynamically from inside-out. This evolutionary phase is characterized by a central protostar and disc, deeply embedded within an infalling envelope of dust and gas. The infalling material passes through an accretion shock as it falls onto the central star and disc, which, along with accretion within the disc, produces the main contribution to the luminosity for low-mass protostars. The emergent spectral energy distributions of theoretical models in the infall stage are in close agreement with those of recently found infrared sources with negatively steep spectra in the near- and mid-infrared. Protostars of high mass, in a pure accretion phase, have yet to be found, although the source near the water masers in W3(OH) is probably close to being such an object. The third stage, as a protostar accretes matter, deuterium will eventually ignite in the central regions and drive the star nearly completely convective if its mass is less than about $2M_{\odot}$. If the convection and the differential rotation of the star combine to produce a dynamo, the star can naturally evolve toward a state with a stellar wind. However, at first the ram pressure from material falling directly onto the stellar surface suppresses breakout. Gradually, the lid of direct infall will weaken as the incoming material falls preferentially onto the disc rather than onto the star. The stellar wind then rushes through the channels of weakest resistance (the rotational poles), which leads to colliminated jets and bipolar outflows. Thus, the protostar enters the next step of evolution the bipolar outflow phase. Examples of massive Young Stellar Objects (YSOs) in this phase of stellar evolution (combine inflow and outflow) include the Becklin Neugebauer object in Orion, but the trigger for the stellar wind in such cases is still theoretically obscure. In the fourth stage, more and more of the rotating inflowing matter will fall preferentially onto the disc rather than onto the star. In any reasonable picture of stellar outflows, the opening angle of the wind will widen with time, eventually sweeping outward over all 4π steradians. In the case of a "low mass YSO", a T Tauri star with a surrounding remnant nebular disc. Radiation from disc adds an

infrared excess to the expected spectral energy distribution of the revealed source. The detailed shape of this infrared excess depends on whether the disc is largely passive and merely reprocessing stellar photons, or whether it is relatively massive and actively accreting. Both extremes of spectral shapes are observed in T Tauri stars; the amount of circumstellar material in the form of discs around nearly formed stars may be related to the dual issues of the origins of binary star and planetary systems. Discs around high-mass YSOs may also be common; in at least one well documented case, S106, the disc is very large spatially but not extremely massive (i.e. not more massive than the central star). The fifth stage, the final disappearance of the nebular disc as matter becomes incorporated into planets or stellar companions or is dispersed by the energetic outflow. For low mass YSOs, such objects are probably the naked T Tauri stars (Mundt et al., 1983; Walter et al. 1986a Walter et al. 1986b).

Observationally, low-mass young stellar objects have been divided into four distinct evolutionary classes on the basis of their spectral energy distributions (SEDs) (c.f. Lada and Wilking, 1984; Andre et al., 1993). Radiation from the powering central source is scattered, absorbed and re-emitted by the dusty protostellar envelope before escaping to interstellar space. The variation in the shape of the resultant SED reflects the conditions in the envelope at each stage of evolution. Figure 2.1 shows the evolutionary sequence and the associated spectral energy distributions for the classes 0 to III.

Class 0: Collapse has commenced at this stage raising the temperature and luminosity of the core. The SED resembles a single blackbody, with a temperature between 20 and 30 K, and so peaks in the sub-millimetre band, at $\lambda > 150\,\mu$m. Many Class 0 sources drive energetic bipolar outflows (Lada, 1999; Andre et al., 1993), implying that the infall is not spherical and disks-like structures have already formed.

Class I: As accretion proceeds the dust temperature rises and the peak of the SED moves to the far-IR ($\sim$100 μm). Residual rotation causes the infalling material to form an accretion disk around the central protostellar object. Bipolar outflows and jets are formed as momentum and energy is bled off into the surroundings. The SED profile corresponds to a 50–100 K blackbody, originating in the accreting envelope, plus additional 200–400 K components, originating in the disk. A silicate absorption feature is often present at 10 μm, indicating an optically thick envelope of dust. Observationally these sources are deeply embedded and invisible at wavelengths shortward of 1 μm.

Class II: After $\sim 10^6$ years, winds and molecular outflows have swept away much of the natal envelope, exposing the dusty disk. The peak of the SED falls in the near-infrared band, around 2 μm. Flux longward of 2 μm is dominated by excess emission from the disk. At this stage, the pre-main-sequence core is often visible in the optical and near-infrared, and is typically identified as a T-Tauri star.

Class III: These objects are visible as stars in the near-infrared and optical, where their SED peaks. Some circumstellar material may be present in the form of a thin disk, however, the SED is generally well fit by a reddened blackbody with little or no IR excess emission. This is consistent with a reddened stellar photosphere of a star on the zero-age-main-sequence.

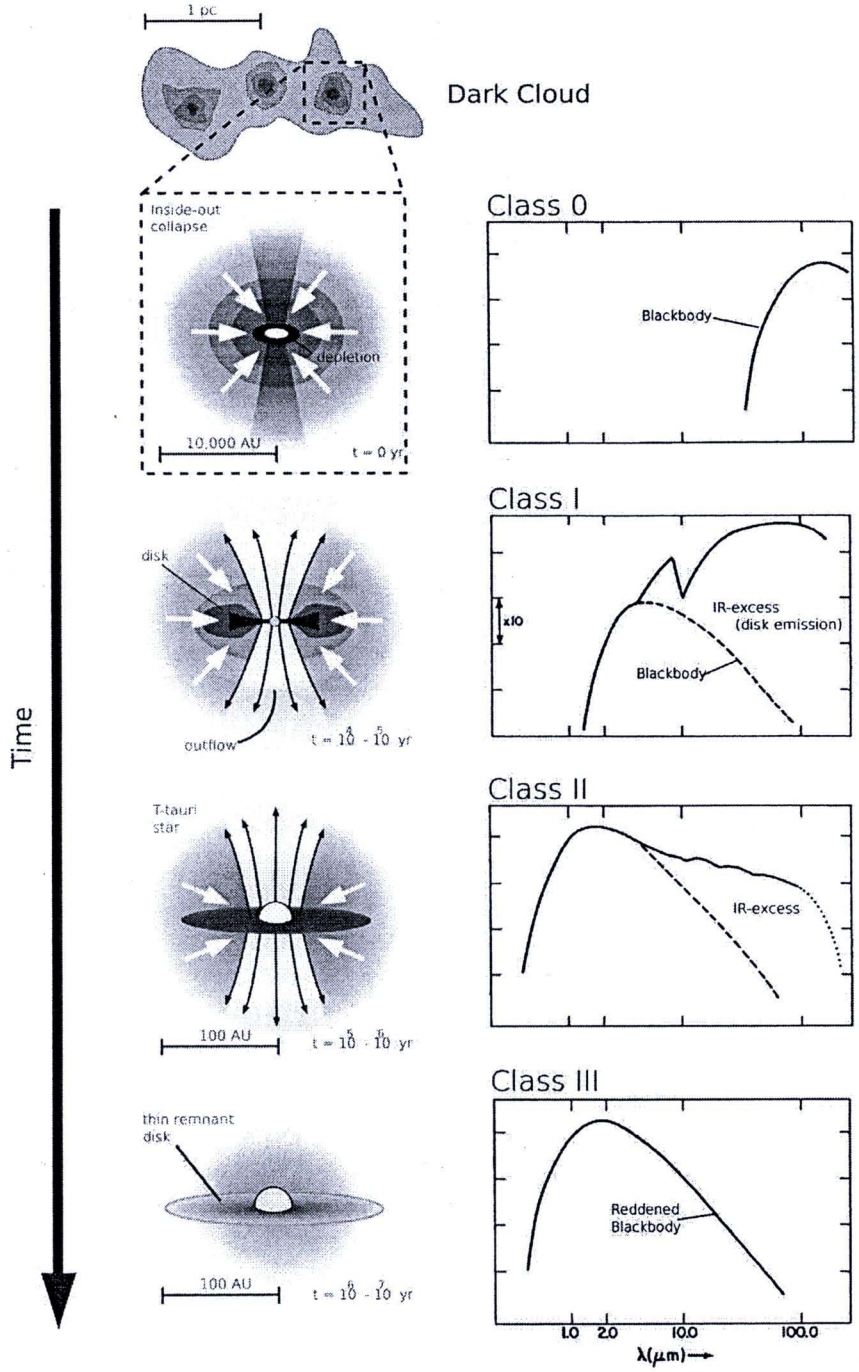

Figure 2.1 Schematic representation of the evolutionary sequence for low-mass stars (taken from Purcell 2007). Initially a dense knot of gas undergoes inside-out collapse, forming a central protostellar core. Residual angular momentum causes the cloud to spin into a circumstellar disk. Accretion via the disk gives rise to bipolar outflows and collimated jets. After $> 10^7$ years the circumstellar material is exhausted and accretion ceases.

The evolution of the SED is due to gradual dissipation of gas and dust from the natal envelope. A quantitative classification scheme is based on the spectral index between 10 μm and 100 μm, according to (Lada, 1987)

$$\mathrm{a} = \frac{\mathrm{dlog}(\lambda\, \mathrm{F}_\lambda)}{\mathrm{dlog}(\lambda)}. \tag{2.1}$$

For class I sources $0 < a \leq 3$, for class II sources $-2 \leq a \leq 0$, and for class III sources $-3 \leq a \leq -2$.

2.1.1.2 High - Mass Star Formation

High mass stars form within dense cores containing at least $8\mathrm{M}_\odot$ of gas concentrated in a region ≤ 0.05 pc, which is the mean separation between stars observed in clusters (Testi et al. 1997 Hillenbrand, 1997; Kurtz et al., 2000). Although massive stars play a role in shaping galactic structure and evolution, our understanding of their formation and early evolution is still very unclear. There are many reasons for this: e.g. high dust extinction makes it difficult to observe high-mass stars during the critical early-formation phases. Moreover, they are rare, evolve quickly, and important evolutionary phases are short-lived. They are seldom (if at all) formed in isolation and the proximity of other highmass stars compounds the complex influence of the local environment (e.g. gravitational interactions, powerful outflows and winds, ionizing radiation and supernovae) on the forming star.

As one might expect, under such circumstances theoretical modelling is extremely complex. If the low-mass star-formation scenario is applied to highmass stars a number of problems are encountered which make the scenario implausible. As mentioned before, high-mass stars form in a time $\geq t_{KH}$, meaning that they begin emitting intense ultraviolet radiation and winds of energetic particles while still accreting material. As maser emission appears to be associated with high-mass star-formation, it should provide a very useful tool for studying the physical properties of high-mass stars and act as an aid to our understanding of their formation.

2.1.2 Physics of Star Formation

In this section, the important physical conditions and criteria which affect and determine star formation will be described. These are hydrostatic equilibrium, the gravitational potential and kinetic energy of a sphere of matter, collapsing clouds, the Jeans criteria, the time-scale for free-fall and angular momentum.

2.1.2.1 Hydrostatic Equilibrium

For a cloud to be stable against collapse or expansion, its internal pressure must exactly balance gravity at all positions in the cloud. This is called *hydrostatic equilibrium*.The conditions of hydrostatic equilibrium can be derived as follows:

Consider a small volume in a static spherical gas cloud of mass M and uniform density ρ, see Fig. 2.2. The inward force on the disk is produced only by gravity, so

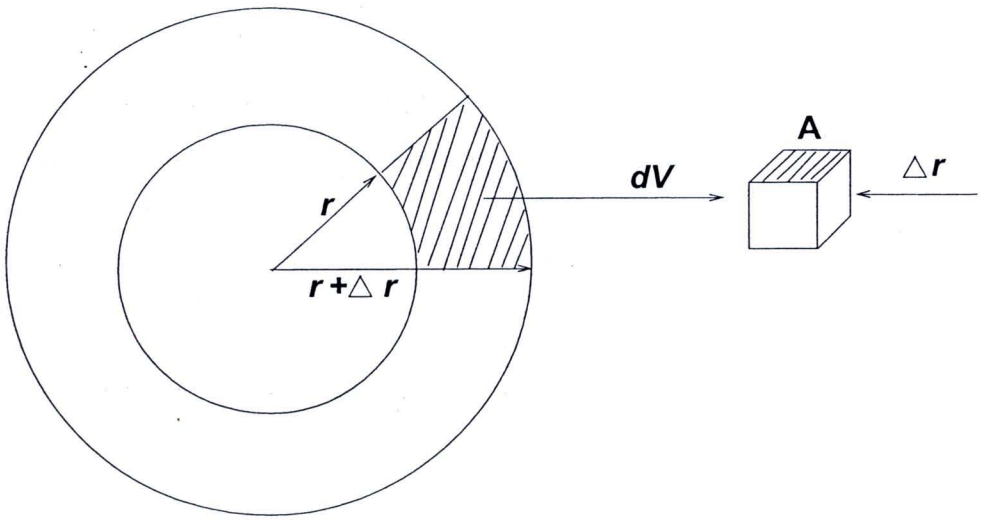

Figure 2.2 Volume element, dV, in a spherical gas shell.

$$F_{in} = -m_d \frac{GM_r}{r^2}, \tag{2.2}$$

where M_r is the mass interior to radius r, F_{in} is inward force, G is the universal gravitational constantand $m_d = A\Delta r\rho$ is the mass of the disk, where A is area of volume, Δr is small radius and ρ is density of a volume element dV as shown in Fig. 2.2.

The outward force, F_{out}, is simply the internal gas pressure, so

$$F_{out} = A\Delta P, \tag{2.3}$$

where F_{out} is outward force and ΔP is the force/unit area on the face of the disk. For equilibrium, we require that

$$F_{out} = -F_{in}, \tag{2.4}$$

$$A\Delta P = -A\Delta r\rho \frac{GM_r}{r^2}, \tag{2.5}$$

$$\frac{\Delta P}{\Delta r} = -\rho \frac{GM_r}{r^2} = -g_r\rho, \tag{2.6}$$

where the acceleration of gravity at position r is $g_r = \frac{GM_r}{r^2}$. Thus,the pressure gradient is balanced by gravity at all points as required by hydrostatic equilibrium. In this treatment, we have neglected effects of rotation, magnetic fields, and bulk motions. Since g_r is always radial, hydrostatic equilibrium in gaseous and fluid objects produce spherical shapes.

2.1.2.2 Gravitational Potential Energy and Kinetic Energy of a Sphere

For systems with a large number of particles such as a molecular cloud, we will think in terms of a fluid with density ρ rather than try to deal with many individual particles (atoms or molecules). In a sphere of constant density ρ, the mass M and radius R are related by

$$M = \frac{4\pi}{3} R^3 \rho. \tag{2.7}$$

The gravitational potential energy is equivalent to the work required to bring all matter of mass M from infinity to the final radius R. To calculate the gravitational potential energy U, we will assemble the sphere one thin shell at a time and add them together.

Consider a shell of thickness $\mathrm{d}r$ at radius r, see Fig. 2.2.
The volume of the shell is

$$\mathrm{d}V = 4\pi r^2 \mathrm{d}r, \tag{2.8}$$

and the mass of the shell is

$$\mathrm{d}M = 4\pi r^2 \mathrm{d}r \rho. \tag{2.9}$$

The total mass interior to r is

$$M(r) = \frac{4\pi}{3} R^3 \rho, \tag{2.10}$$

if ρ is constant. The gravitational potential between any two points separated by distance r is

$$U = -G m_1 m_2 / r. \tag{2.11}$$

The work required to add the mass $\mathrm{d}M$ to $M(r)$ is

$$\mathrm{d}U(r) = -\frac{GM(r)}{r} \mathrm{d}M = -G \left(\frac{4\pi}{3} \right) 4\pi \rho^2 r^4 \mathrm{d}r. \tag{2.12}$$

Thus the total work required to assemble the entire sphere is

$$U = \int_0^R \mathrm{d}U(r) \tag{2.13}$$

$$= -G(4\pi/3)4\pi\rho^2 \int_0^R r^4 \mathrm{d}r \tag{2.14}$$

$$= -\frac{3}{5} \frac{GM^2}{R}. \tag{2.15}$$

The thermal energy per particle in a gas cloud is

$$E_{th} = \frac{3}{2} NkT, \tag{2.16}$$

where N is the total number of particles in the cloud. If μ is the mean mass per particle, then $N{=}M/\mu$ and

$$E_{th} = \frac{3}{2} \frac{M}{\mu} kT. \tag{2.17}$$

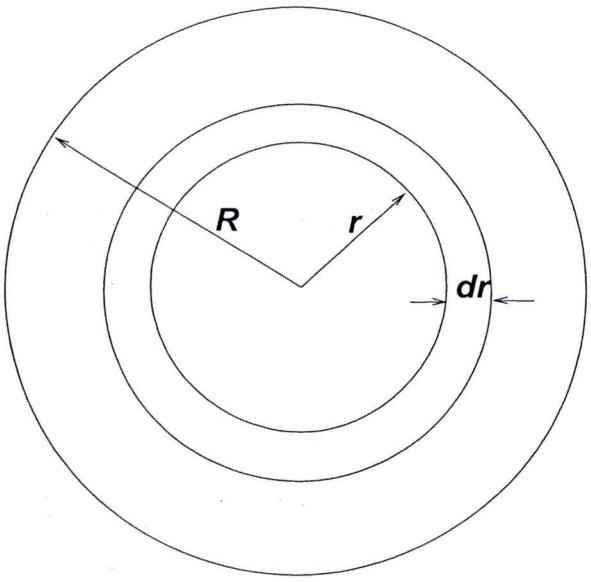

Figure 2.3 Volume model.

2.1.2.3 Collapsing Clouds

From the virial theorem,

$$-2K = U, \tag{2.18}$$

if twice the total internal kinetics energy of a molecular cloud (2K) exceeds the absolute value of the gravitational potential energy ($|U|$), the force to the gas pressure will dominate over the force of gravity and the cloud will expand. On the other hand, if the internal kinetic energy is too low, the cloud will collapse. Now that, by the virial theorem, the condition for collapse ($|U| \geq 2K$) becomes

$$\left| \frac{-3}{5} \frac{GM^2}{R} \right| \geq 3kT \frac{M}{\mu}, \tag{2.19}$$

which implies that

$$\frac{M}{R} \geq 5 \frac{kT}{G\mu}, \tag{2.20}$$

Recall that M and R are not independent since they are related via the density relation: $\rho = M/\left((\frac{4\pi}{3})R^3\right)$.

2.1.2.4 The Jeans Criteria

Let us now try to estimate the smallest cloud of a given density ρ, mean mass per particle μ and temperature T for which the gravitation and kinetic energies

are just equal, that is the point at which the cloud is just balanced between gravity and thermal energy. Note that we neglect turbulent motions, rotation, magnetic, pressure, and other bulk motions, thus the equilibrium radius that we derive here will be a lower limit. In practice, the radius that we derive is probably a factor or 2 or more underestimated.

We have in our idealized case:

$$\frac{M}{R_j} = 5\frac{kT}{G\mu}, \tag{2.21}$$

or

$$\frac{4\pi R_j^3 \rho}{3R_j} = 5\frac{kT}{G\mu}, \tag{2.22}$$

where R_j is the Jeans Radius or the radius at which E_{th} and U are equal. Solving for R_j:

$$R_j = \left(\frac{15kT}{4\pi\mu\rho G}\right)^{\frac{1}{2}}, \tag{2.23}$$

It is often convenient to express the $\frac{M}{R}$ relation in terms of the *minimum mass* or *Jeans Mass;* M_j for which a cloud of ρ,μ, and T will be just gravitationally stable. This can be done as follows:

$$M_j = \frac{4\pi}{3}R_j^3\rho, \tag{2.24}$$

$$= \frac{4\pi}{3}\left(\frac{15kT}{4\pi\mu\rho G}\right)^{\frac{3}{2}}\rho, \tag{2.25}$$

$$\approx \left(\frac{5kT}{\mu G}\right)^{\frac{3}{2}}\left(\frac{3}{4\pi\rho}\right)^{\frac{1}{2}}, \tag{2.26}$$

or in terms of gas volume $n = \rho/\mu$,

$$M_j \approx \left(\frac{5kT}{\mu G}\right)^{\frac{3}{2}}\left(\frac{3}{4\pi\mu n}\right)^{\frac{1}{2}}. \tag{2.27}$$

2.1.2.5 Free-Fall Time Scale

Once a cloud becomes gravitationally bound, it will begin to collapse. We now want to estimate how long it will take to collapse to stellar size if unimpeded by other forces.
The acceleration of a particle at radius r is:

$$a(r) = GM_r/r^2 = \frac{4\pi}{3}r\rho G,$$

or

$$\frac{1}{r}\frac{d^2r}{dt^2} = \frac{4\pi}{3}r\rho G.$$

Solving this equation of motion for the time which we will call t_{ff},(Free-Fall Time):

$$t_{ff} = \left(\frac{3\pi}{32G\rho_0}\right)^{\frac{1}{2}}, \tag{2.28}$$

where ρ_0 is the initial density. Note that the free-fall time depends only on the density and not the cloud mass. It is also independent of starting radius.

2.1.2.6 Angular Momentum

If the initial cloud out of which a star formed has any small amount of net angular momentum, as any real cloud will surely have (due to galactic rotational shear, and other bulk motions), then this will be conserved as collapse proceeds. The angular momentum,L, is given by:

$$L = I\omega, \tag{2.29}$$

where I is the moment of inertial and ω is the angular speed of the cloud. For a sphere:

$$I = \tfrac{2}{5}Mr^2 \text{ and } \omega \propto \tfrac{1}{r^2}.$$

If I_0 and ω_0 are the initial values, then $I_0\omega_0 = I\omega$ at any other time from the conservation of L. From which we infer that

$$\frac{\omega}{\omega_0} = \left(\frac{r_0}{r}\right)^2. \tag{2.30}$$

This implies that the radial acceleration of a test particle of mass m at radius r will have two components

1) gravity: $a_g(r) = GM(r)/r^2$ which directed *radially toward the center*, and

2) a centripetal term $a_c(r) = r\omega^2$ directed *away from the axis of rotation*.

The radial component of $a_c(r)$ is

$$a_c(r) = r\omega^2 \sin\phi, \tag{2.31}$$

where ϕ is the angle from the axis of rotation to the particle as seen from the center, see the drawing in Fig. 2.4. Thus the net radial acceleration is

$$\begin{aligned} a(r) &= a_g(r) + a_c(r), & (2.32)\\ &= \frac{GM(r)}{r^2} - r\omega^2 \sin\phi. & (2.33) \end{aligned}$$

This shows that $a(r)$ is small for a rotating cloud than for a non-rotating cloud. Further, at the pole ($\phi = 0°$),$a(r) = a_g(r)$ only, but at the equator ($\phi = 90°$)

$$a(r) = a_g(r) - r\omega^2, \tag{2.34}$$

Now let us look at the both accelerations are dependency on r for matter in the equatorial. Assume that the mass interior to our contracting mass point is constant (i.e.$\rho \propto \frac{1}{r^3}$)

$$a_g \propto \frac{1}{r^2}.$$

and

$$a_c \propto r\omega^2 \propto \tfrac{1}{r^3}.$$

Thus as r decreases,a_c increases faster than a_g and as contraction proceeds, at some point a_c will become equal to and then larger than a_g. At the point where $a_c = a_g$, the gas cannot contract any closer to the center. Contraction can continue *out* of the equatorial disk, but not in the disk.
We will now work out how much the cloud contracts before $a_c = a_g$. We start with the following equation,

$$\frac{GM(r)}{r^2} = r\omega^2, \tag{2.35}$$

thus,

$$GM(r) = r^3\omega^2. \tag{2.36}$$

Subsitute $\omega = (r_0/r)^2\omega_0$ into equation (2.36), we obtain,

$$GM(r) = r^3\omega_o^2(r_0/r)^4, \tag{2.37}$$

$$= (r_0\omega_0)^2\left(\frac{r_0}{r}\right)r_0, \tag{2.38}$$

as $v_0 = \omega_0 r_0$ then

$$GM(r) = v_0^2 r_0(r_0/r), \tag{2.39}$$

we can now obtain that

$$\frac{r}{r_0} = \frac{v_0^2 r_0}{GM_{(r)}}, \tag{2.40}$$

where v_0 is an orbital velocity.

As collapse proceeds an initially large, massive cloud will flatten around the equatorial plane. Matter in the equatorial disk (accretion disc) can contract only so far until it is stopped by rotation. At this point, the cloud is likely to fragment into smaller pieces of higher density. These fragments can then contract further until they reach their into orbital motion leaving the fragments left behind to contract further. This process probably until fragments of about Jeans mass and radius are formed, at which point the process of star formation can take place. This is why most stars are formed as part of a starcluster rather than as individual isolated stars.

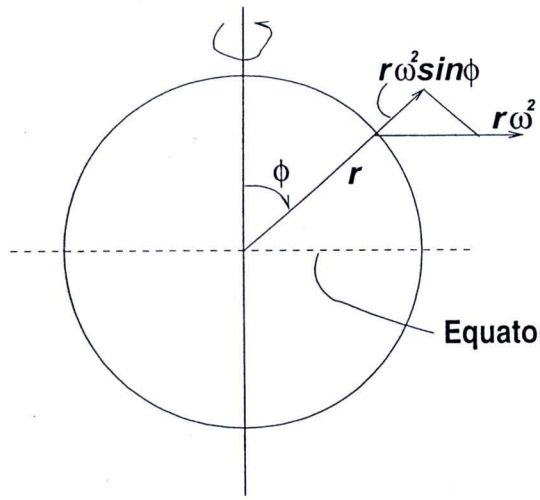

Figure 2.4 Shown angle ϕ from the axis to the particle as seen from the center.

2.1.3 Accretion Disc

As has already been indicated, accretion discs play an intrinsic role in star-formation. As a disc forms and gravitational forces further compress the material, it will start to radiate at frequencies dependent upon the mass of the central object. For young stars and protostars, this is in the infra-red. The presence of the star, forming at the centre of the axis of rotation, will also mean that the material in the disc will approximately follow Kepler's laws of motion since the star's mass will be dominant: i.e. the circular speed, V, of the material at a distance, R, from the axis of rotation, is given by,

$$V = \sqrt{\frac{GM}{R}}, \tag{2.41}$$

where G is Newton's gravitational constant, and M is the mass interior to R, which is essentially that of the star.

For a Mestel disc, with an assumption of no central condensation and therefore a better description of an unevolved object, it is possible to show that the mass enclosed within a radius R of $M(R)=2\pi \int_0^R \Sigma(R')R'dR'$ (Binney and Tremaine, 2008) and surface density $\Sigma(R') = \Sigma_0 R_0/R'$ so that $M(R)=2\pi\Sigma_0 R_0 R$. The circular speed is $V_c^2(R) = \frac{GM(R)}{R}$, so that $M(R)=\frac{RV_c^2}{G}$. The two formulae for M(R) imply that the circular speed is independent of radius.

2.2 Bipolar Outflows

All stars pass through an outflow stage as fundamental part of the star formation process (see the reviews by Lada, 1985; Welch et al. (1985) and Snell, 1987). The outflows are highly energetic (observed kinetic energies are 10^{43}-10^{47}

erg) and exhibit a wide variety of observable phenomena. Related manifestations include Herbig Haro (H-H) objects (see the review by Schwartz, 1983), high velocity maser sources and "cometary" reflection nebulae etc. The molecular outflows (which occur in YSOs of all masses) may also be driven by strong stellar winds. The case for stellar winds is supported by the claim that the CO gas in the bipolar lobes of L1551 exists in spatially thin shells (Snell and Schloerb, 1985; Kaifu, 1987).

At present, astronomers believe that magnetic fields in accretion disks have a crucial role in producing the outflows or jets observed in many protostellar objects. In turn, the outflows may have a key role in removing angular momentum from the inner regions of the disk (Brebner et al., 1987; Hutawarakorn et al., 2002; Hutawarakorn and Cohen, 1999; Hutawarakorn and Cohen, 2003; Hutawarakorn and Cohen, 2005) thereby facilitating the accretion of matter onto star. The best known theoretical models and ideas are Pudritz & Norman model and Uchida & Shibata model.

Pudritz (1983) and Pudritz and Norman (1986) (see also Pudritz, 1985) proposed a scenario in which an hour glass shaped poloidal field co-rotates with the disk (see Fig. 2.5). Partially ionized material is centrifugally accelerated away from the disk plane along the magnetic field lines,thus removing angular momentum and driving accretion. Pudritz and Norman (1986) suggested that an ionized disk wind originates from a disk of radius r $<$ 70 AU, whilst the molecular outflow originates from a magnetised disk with radii between 70 AU and 7000 AU.Therefore angular momentum is removed from the inner part of the disk, increasing the accretion rate.

Uchida et al. (1985) suggested that a toroidal field is built up near the disk surface by a rapidly contracting and differentially rotating disk which wraps up the threading poloidal field. This produces a magnetic pressure gradient directed away from the disk, and so gas is pushed away in the polar directions to create the bipolar outflow, and again removing angular momentum. The schematic picture illustrating the situation under consideration in their model is as in Figure 2.6

Proposed mechanism for colliminating jet and bipolar molecular flows fall into two generic categories. One viewpoint is the outflows are produced in a well collimated form near the star (e.g. Hartmann and MacGregor, 1982; Jones and Herbig, 1982). The other viewpoint is an initially isotropic stellar wind is channeled into a bipolar form by an anisotropic distribution of matter in the surrounding circumstellar environment (e.g. Canto et al., 1981; Konigl, 1982; Torrelles et al. 1983, see also Heyer et al., 1986). Massive outflows can either be jetlike or present low collimations (wide opening angles), similarly to what is found in the case of low mass stars (Kumar et al., 2002; Beuther et al., 2004). High spatial resolution observations of various massive outflows show that very collimated jetlike structures do exist at the earliest evolutionary stages of high mass star formation and change with time (Beuther et al., 2004). Massive outflows get distorted and broken into pieces as they encounter the dense environment around the members of a tight cluster or nearby companion that are associated with luminous young stars (Kumar et al., 2002). The comparisons of position velocity diagrams with data from low mass sources show that similar kinematic structure

for outflows of all masses, and that jet driven as well as wind driven models are necessary to explain all features. For the high mass source estimate accretion rates to a few times 10^{-4} $M_{\odot}$ yr^{-1} (Beuther et al., 2004).

2.3 Astronomical Masers

2.3.1 Introduction to Masers

A Maser is a phenomenon similar to a laser, except that the word 'MASER' is derived from Microwave Amplification by Stimulated Emission of Radiation, the word 'Light' being replaced by the word 'Microwave' in the derivation of the word 'LASER'. They arise naturally in space when interstellar molecules interact with systems at several different temperatures. As such, they are called Interstellar Masers. In some cases, the energy level populations become inverted, perhaps by infra-red or collisional pumping, and stimulated emission can occur, resulting in amplification of the stimulating radiation. This amplification should be exponential because each stimulating photon causes the emission of an identical photon in the same direction as the stimulating radiation. However, the increase in intensity is not exponential because the stimulated emission tends to reduce the energy level population inversion. A maser is said to be saturated when the stimulated emission rate is comparable to or greater than the intrinsic pumping rate.

2.3.1.1 Occurence of Masers in Space

Interstellar masers appear to be a signpost of young high-mass star-forming regions, and can therefore be used as powerful probes of the physical conditions in these regions, such as temperature, density, molecular abundance etc. (Cragg et al., 2001; 2002; Gray 2007 and references therein). They also occur in the circumstellar envelopes of evolved stars, in comets and in planetary atmospheres. The most commonly observed masers are from water (H_2O), the hydroxyl (OH) radical and methanol (CH_3OH), but others from molecules such as silicon monoxide (SiO), formaldehyde (H_2CO) and ammonia (NH_3) have been observed in more than one source.

It would appear that methanol, OH, and water masers are frequently found in the same sources, although water and methanol masers usually originate in different regions of them (Beuther et al., 2002; Caswell, 2004; Edris et al., 2005; Szymczak et al. 2005). Most sources with 6.7 GHz methanol masers seem to have associated OH masers, almost always at 1665 MHz and frequently also at 1667 MHz (Szymczak et al. 2004), while the correlation between 6.7 GHz methanol masers and 22 GHz water masers is less strong (Breen et al., 2007). The distributions of the 6.7 GHz methanol masers and the 6.0 GHz OH masers in W3(OH) are very similar, although a direct overlap of the two species is rare (Etoka et al., 2005). Similar phenomena are also seen between 6.7 GHz methanol and 1.6 / 4.7 GHz OH masers (Harvey-Smith and Cohen, 2006).

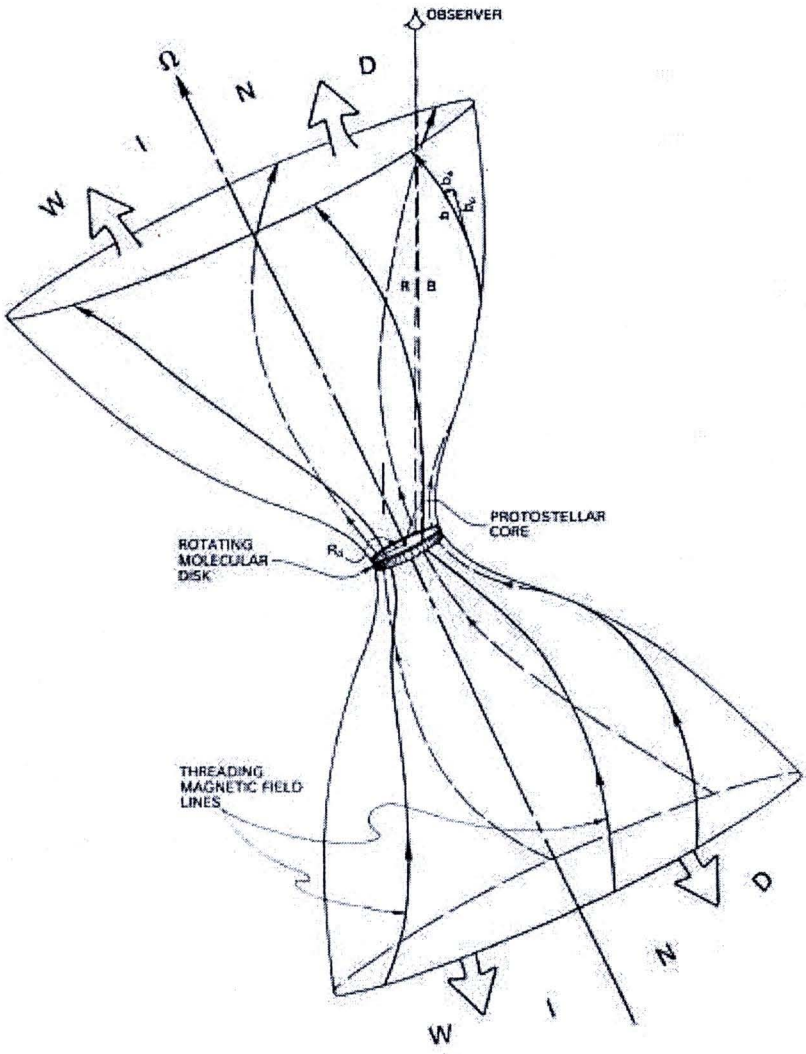

Figure 2.5 The conceptualization by Pudritz & Norman (1986) of a bipolar outflow driven off a circumstellar accretion disk and centrifugally accelerated by a strong magnetic field.

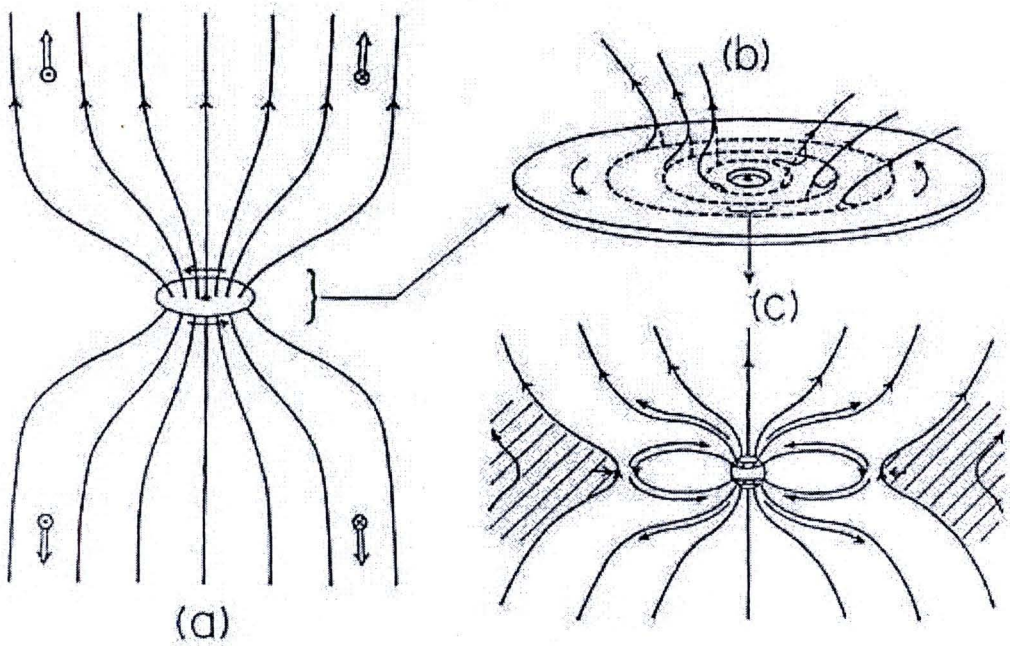

Figure 2.6 Schematic illustration of the model of Uchida et al. 1985. (a) A part of the cloud condenses into a rotating disk,bringing a part of the large scale magnetic filed into it. The filed lines will be twisted around the axis of rotation. (b) Enlarged view of the rotating disk which twists the magnetic field lines. (c) Further enlargement of the region near the central object. The magnetic field structure has a magnetically neutral ring around the star as long as both the stellar and disk magnetic fluxes come from the same large scale magnetic filed of the cloud (and if the self regenerative dynamo effect which may invert the magnetic polarities of the poles has not yet started).

2.3.1.2 Individual Molecules Forming Masers

a) Hydroxyl (OH) Masers and their classification Hydroxyl or OH masers are usually studied in sources with associated UCHII regions (Fish et al., 2005) but are also found toward less evolved massive protostellar objects (Edris et al., 2007). A different class of OH masers is seen at the ends of the jet in the W3 TW object (Argon et al., 2003). Moreover, the OH masers are found around the evolved sources in expansion (sometimes very rapid; see Stark et al. (2007) ahead of the ionization front of a UCHII region (Fish and Reid, 2006). Sometimes the masers appear to trace a molecular disc or torus (Slysh et al., 2002; Hutawarakorn and Cohen, 2005; Edris et al., 2005; Nammahachak et al., 2006). Masers are often seen along arcs or filaments (Cohen et al., 2006), with extended filamentary emission especially common at 4.7 GHz (Palmer et al., 2003).

The OH maser has been detected from nine lambda doublet, hyperfine transitions in the $^2\prod_{3/2}$ and $^2\prod_{1/2}$ rotational ladders (see Moran 1976). The strongest OH maser comes from the ground state transitions ($^2\prod_{3/2}$, $J = 3/2$). There are two main-line transitions, the $F = 1 - 1$ transition at 1665.402 MHz (see Figure 2.7) and the $F = 2 - 2$ transition at 1667.359 MHz, and two satellite-line transitions, the $F = 1 - 2$ transition at 1612.231 MHz and the $F = 2 - 1$ transition at 1720.530 MHz. A classification scheme for OH masers was developed by Turner (1970, 1979) . This is based on regularities in the OH ground-state line radios, line shapes and polarization of galactic sources. Sources in which the OH mainlines (1665 and 1667 MHz) dominate are type I, and sources in which the OH satellite lines (1612 and 1720 MHz) dominate are type II in this scheme. Type I sources are usually associated with regions of star-formation and usually strongest in the 1665 MHz transition stronger in 90% of cases Caswell and Haynes (1987). Satellite line emission at 1612 or 1720 MHz is generally weaker and has only been detected in ~15% of sources. Given the wide range of maser lines now know, such a classification seems unduly restrictive.

Emission from the first two excited states of OH was discovered (Zuckerman et al. 1968; Yen et al. 1969) for the $^2\prod_{1/2}$, J=1/2 and $^2\prod_{3/2}$, J=5/2 states, respectively). The $^2\prod_{3/2}$, J=5/2 excited state of OH lines immediately above the ground state. This state gives rise to four hyperfine transitions, with the F = 3 – 3 and F = 2 – 2 main lines at 6035.092 and 6030.747 MHz and the F = 3 – 2 and F = 2 – 3 satellite lines at 6049.084 and 6016.746 MHz, respectively (see Figure 2.7). In addition, these transitions are sensitive to the magnetic field with a Landé factor $g_J = 0.485$ (Davies, 1974).

The field strengths are obtained from Zeeman splitting and the orientation of the field to the line of sight can be estimated from linear polarization measurements, so the three-dimensional structure of the magnetic field could be derived. This idea has been used in the recent

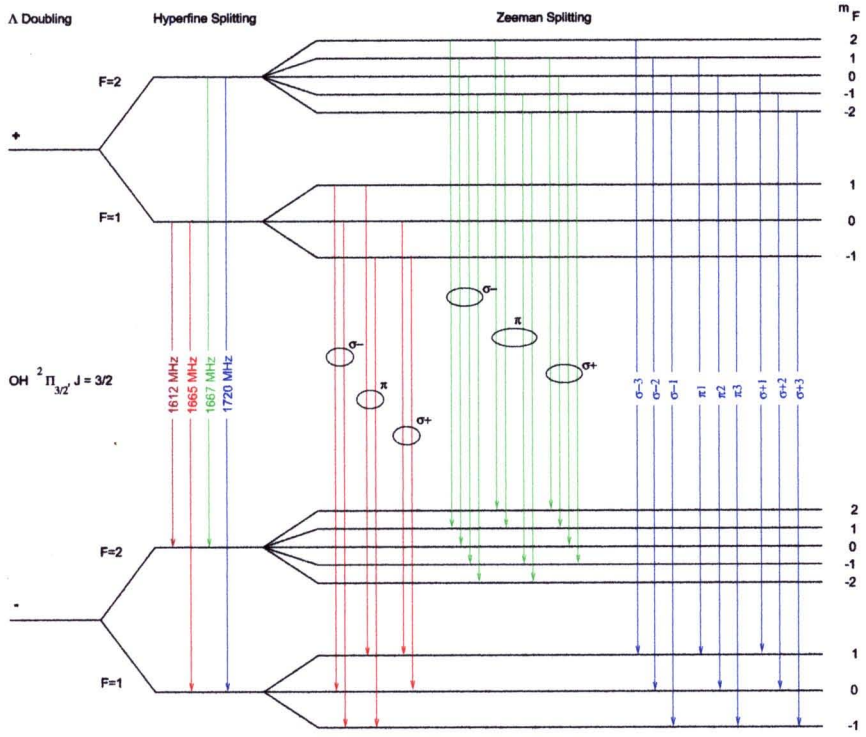

Figure 2.7 The energy level of OH masers (taken from Hutawarakorn 1997).

MERLIN observations to observe in many sources such as ON1 (Green et al., 2007; Nammahachak et al., 2006) and W3(OH) (Etoka et al., 2005). Magnetic fields obtained from those regions had typical values from −0.4 to +14.4 mG except that in some cases fields as strong as +40 mG are seen in OH masers (Slysh and Migenes, 2006; Fish and Reid, 2007). While magnetic field strengths are usually stable from epoch to epoch, monotonic decay of the field in a Zeeman group in Cep A continues to be observed (Bartkiewicz et al., 2005).

b) **Methanol (CH_3OH) and their classification** Methanol masers can be divided into two categories, Class I and Class II, the Class I masers being primarily collisionally pumped, whereas the Class II masers are radiatively pumped. The main difficulty in studying Class I methanol masers 29 has been the lack of good criteria on which to base targeted searches, although Ellingsen (2005) has shown that approximately 40% of Class II methanol masers have an associated Class I maser within 30 arcsec. Although, in theory, strong Class I and Class II masers cannot co-exist, Figure 2.9 shows the 95.1 GHz Class I masers towards the well-known Class II maser source, G328.81+0.63. There is Class I methanol maser emission from the same projected location as the Class II masers, and they extend over the same velocity range. In fact, Class I masers are typically associated with young sources and also seem to trace distant

parts of outflows interacting with dense molecular gas (Beuther et al., 2005; Ellingsen, 2006). Class II methanol masers, the main transitions of which have frequencies at 6.668 GHz and 12.178 GHz, seem to be uniquely associated with massive star-formation (see Niezurawska et al. 2005). They are also found in regions at an earlier evolutionary stage than that of the ultra-compact (UC) HII regions (Minier et al., 2005) and can also be found in discs (Norris et al., 1993; 1998) and outflows (Fish, 2007).

c) **Water (H_2O) Masers** The predominant and easily observable water maser line, arising from the 6_{16} - 5_{23} rotational transition in the water molecule at a frequency of 22.235 GHz (Babkovskaia and Poutanen, 2004), is frequently seen in outflows from both high-mass and low-mass YSOs (Felli et al., 1992; Honma et al., 2005; Goddi and Moscadelli, 2006; Moscadelli et al., 2006). The line of sight magnetic fields of tens to hundreds of milligauss have been measured in star-forming regions via water maser Zeeman splitting (Sarma et al., 2002; Vlemming et al. 2006). A recent survey of water maser emission towards the G333.6-0.2 giant molecular cloud (Breen et al., 2007) complements previous unbiased surveys of 6.7 GHz methanol (Ellingsen et al., 1996) and main-line OH masers (Caswell et al., 1980) in the same region. Figure 2.8 shows that all the water masers lie very close to the main axis of the cloud, as traced by the bright mid-infrared emission, whereas the methanol masers generally lie near the interface between the stronger and more diffuse emission. This suggests that 6.7 GHz methanol masers trace an earlier evolutionary phase of high-mass star formation than do luminous water masers.

d) **Formaldehyde (H_2CO) Masers** Formaldehyde masers are seen near a handful of several massive YSOs, with several new detections in recent years (Araya et al. 2005, 2006). They have both a compact and an extended component with velocity gradients (Hoffman et al., 2003; Hoffman et al., 2007). A short-duration flare has been detected toward one source (Araya et al., 2007).

e) **Silicon monoxide (SiO) Masers** SiO masers are commonly seen in evolved stars and are rarely found in star forming regions. They have been seen in bipolar outflows in W51 IRS 2 and Orion KL source I and appear much closer to the central source than do water masers (Eisner et al., 2002; Greenhill et al., 2004). As is the case in evolved stars, the maser species SiO, water, and OH occur at progressively larger distances from source I (Cohen et al., 2006). In the region source I, OH masers do not appear but SiO and water masers do. Moreover, the $v = 1$, $J = 2 \rightarrow 1$ masers are found closer to the protostar in source I than are the $J = 1 \rightarrow 0$ masers, a finding that is difficult to understand in the context of SiO maser pumping models (Doeleman et al., 2004).

f) **Other species** The $(J, K) = (6, 6)$ ammonia (NH_3) maser has been detected centered on a millimeter peak in NGC 6334 I (Beuther et al.,

2007). Weakly inverted acetaldehyde (CH_3CHO) has been detected in the $1_{11} \rightarrow 1_{10}$ transition at 1065.075 MHz toward Sgr B2 (Chengalur and Kanekar, 2003).

2.3.1.3 An Evolutionary Sequence for Masers

At present there remains significant uncertainty about the location within star-forming regions of the different maser species and their evolution. De Buizer et al. (2005) suggest that the different maser species trace a variety of stellar phenomena and are hence associated with multiple evolutionary phases. From recent statistical studies of large samples of maser sources, it appears that:

- Water masers generally trace an earlier evolutionary phase than do OH masers (Forster and Caswell, 1989).
- OH and methanol masers are observed and found in the same regions, although there is no coincidence between the individual maser spots of the different species (Menten et al., 1992; Harvey-Smith and Cohen, 2006; Etoka et al., 2005).

As already noted in discussing the location of water and Class II methanol masers, Ellingsen (2007) have suggested that 6.7 GHz methanol masers trace an earlier evolutionary phase of high-mass star formation than do luminous water masers, from which they have proposed an evolutionary sequence for masers in star-forming regions as shown in Figure 2.10. This sequence shows the general properties of masers in high-mass star forming regions, although some sources do not fit into this sequence. Nevertheless, it usefully describes a majority of cases.

2.3.1.4 The Co-Propagation of OH and Methanol Masers

As already noted earlier, masers are an ideal tool for deriving the physical conditions such as the density and kinetic temperature in star-forming regions. There are two principal requirements for their observation:-

- they need to be observed at as many frequencies as possible to better constrain the set of conditions responsible for the emission.
- it must be established that the observations at the different frequencies come from masers that are co-propagating through the same body of gas.

This second requirement means that absolute positions of the maser spots in the different observing bands are required to an accuracy comparable with that of the resolved size of the spots themselves. This can only be achieved by the use of high-resolution interferometer networks, such as MERLIN, in which observations of the target sources are phase-referenced to phase calibration sources whose absolute positions are accurately known. The separation in the sky of the target and calibration sources must also be $\leq 5^\circ$ because of phase variations with angular separation caused by the atmosphere. Gray et al. (1992) have investigated theo-

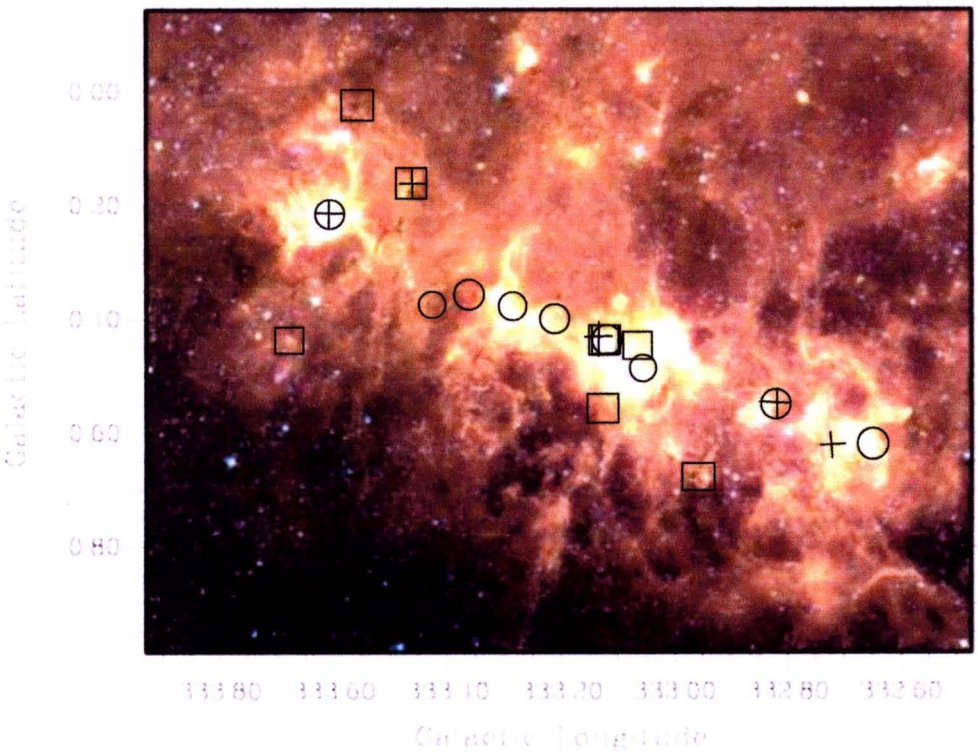

Figure 2.8 Three colour GLIMPSE image of the G333.2-0.6 GMC where red=8.0-μm green=5.8-μm and blue=3.6-μm. The positions of the nine water masers detected in this survey are represented by circles, positions of the methanol masers observed by Ellingsen (2005) are represented by squares and the positions of the OH masers observed by Caswell (1998) are represented by crosses. Water maser sources 1-9 are numbered in order of increasing galactic longitude (taken from Breen et al. 2007).

Table 2.1 Physical conditions for co-propagation of OH masers, from Gray et al. (1992).

Parameter	1720 & 4765	1720 & 6035	1665 & 1667	6035 & 6030
n_{H_2} (cm^{-3})	2×10^7	6×10^6	6×10^6	2.5×10^7
n_{OH} (cm^{-3})	200	60	60	200-250
T_k (K)	125	50-75	50	75
T_d (K)	125	50	50	50
T_x (K)	175	100-125	100	125
v (km s^{-1})	0.67	0.0	2.0	0.0

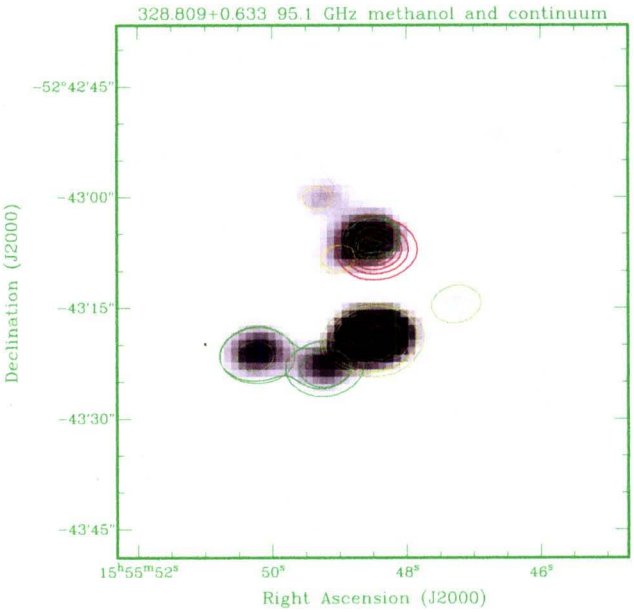

Figure 2.9 G328.81+0.63 shows strong (400 Jy) class II methanol maser emission projected against the ultra-compact HII region (red contours - centred at approximately α = 15:55:48.5, δ=-52:43:07). The greyscale image shows the integrated 95.1 GHz class I methanol maser emission and the contours are a renzogram representing the velocity of the emission (taken from Ellingsen et al. 2007).

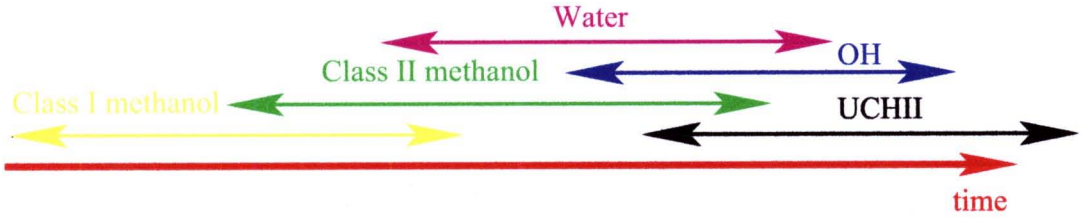

Figure 2.10 A "straw man" evolutionary sequence for masers in high-mass star formation regions (taken from Ellingsen et al. 2007).

retically the conditions that must exist for maser co-propagation. Their modelling has shown that associations between several pairs of OH masers are possible. The physical conditions associated with the existence of lines at paired frequencies are listed in Table 2.1. It can be seen in this table that there are two 'families' of pairs, the first being the 4765/1720 MHz pairing, which requires warm gas and dust at over 100 K. A substantial external radiation field from dust at 175 K is also present. The second family contains all the other pairs, including the ground-state and 6 GHz main lines, and also the 1720/6035 MHz pair. The conditions that support this family include modest kinetic and dust temperatures (T_k and T_d) in the range 50-75 K. The external radiation fields between 100 and 125 K are also lower than those required for the 4765/1720 MHz pair.Within this second family, the strength of the OH lines is determined by the number density of OH and the velocity shift through the maser column: for example, the excited-state main-line pair requires higher OH abundance than the ground-state main-line pair, as would be expected.

A second modelling published by Cragg et al. (2002), has shown that both OH and methanol require very similar high-density, low temperature regimes (dust temperature exceeding 100 K, gas temperatures < 100 K, and densities in the range $10^5 < n_H < 10^{8.3}$ cm^{-3}). A plot showing the approximate regions of parameter space for maser emission for a dust temperature of 175 K is given in Figure 2.11.

From theoretical through observation works, there are some observations as follows allow them compare the co-propagation between OH in many frequency lines with respect to methanol masers at 6.7 GHz in the massive star-forming region. For example, Green et al. (2007) observed OH maser at the excited state 6.0 GHz and 6.7 GHz methanol maser toward ON1 star-forming region and compared the distribution of maser in the same scale with previous work (Nammahachak et al., 2006). They found that there is no association between the 6.7-GHz methanol and the 6-GHz excited-state OH (the closest emission peaks are separated by ~23 mas, even taking into account the deconvolved component sizes there is still distinct separation). The fact that there is only one case of coincidence of all the features shows the physical conditions of the main group of maser spots must vary from the offset coincident pair. From Green's work, they suggested one possibility could be checked the condition between 1612 MHz and the 6035 MHz.

On the other hand the two transitions could be tracing higher density gas, but not to spatially coincident, and so exist in different temperature regions. Based on Modelling of Gray et al. (1992) suggest that the 1612-MHz transition requires kinematics temperatures of $T_k = 150$ K and hydrogen number density 6×10^6 cm^{-3}. Figure 2.11 also implies that a higher density is required for both to be present, but if the dust temperature is consistent, the kinematic temperature regime vary. It is also possible to conclude that the possible spatial separation between the ground and excited state OH (with the exception of the one 1612 MHz feature), could mean we see the very highest density of OH in the excited state regions, as the conditions for excited state OH maser emission extend to higher densities than the ground state. As the methanol lies in the same, slightly offset, region of 6035 MHz omission it too perhaps is in a similarly high-density regime. However of course if both the gas density and temperature are high, then the collision rate

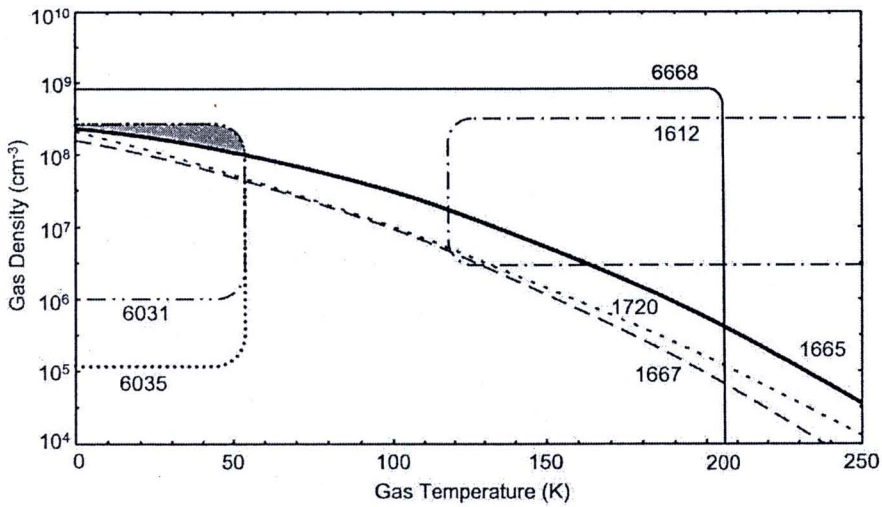

Figure 2.11 Approximate parameter space plot of gas kinetic temperature versus gas density for the OH and methanol maser transitions. Allowed regions are those enclosed by the lines and the axes. The shaded region represents the temperatures and densities for which excited-state OH masers are seen, but ground-state OH is not. The plot is adapted from the results of Cragg et al. (2002) and Cragg et al. (2005), based on a dust temperature of 175 K. It must be noted that several other factors not incorporated in this plot are important for maser emission, such as velocity-coherent column density, fractional number density and optical depths for the infrared radiation.

will be increased and both species of maser are likely to be quenched. Combined with the 1612 MHz distribution, this would lead to the assumption the excited state OH traces the slightly cooler, dense gas, the 6668 MHz methanol the hotter dense gas and the 1612 MHz tracing possibly the hottest dense gas (although the abundance of the molecular species and dust temperature may also vary). The highest density region could be indicative of a shock front, propagating away from the UCHII.

The second example is Etoka et al. (2005), they observed the OH maser at the excited state 6.0 GHz and 6.7 GHz methanol maser toward W3(OH) star-forming region and compared the distribution of both species with previous work (Wright et al. 2004a,b). They found that OH 6.0 GHz masers are frequently associated with 1.7 GHz masers, the closest association being between 6035 and 1665 MHz. Close associations between individual OH 6.0 GHz and methanol 6.7 GHz maser spots in W3(OH) are rare, despite the general similarities between the distributions of the two species at the 0.1-arcsec scale. Moreover, they have searched for the 1665/6035 MHz association using the accelerated lambda iteration method of radiation transfer (Scharmer and Carlsson, 1985) in a slab geometry. Using data computed at $T_k = 60$ K, they found the second family of maser pairings (as defined in Table 2.1) particularly strong at zero velocity shift along the line of sight. However, a wider search of the parameter space is not warranted at this stage, just given the limitations of the observation data only. From theoretical works by Cragg et al. (2002) has established that, given sufficient abundance, methanol and OH masers appear under the sago physical conditions. These are indications that methanol may peak in abundance before OH does, in the evaporation of both species from dust mantles. Cragg et al. suggest that could provide a new form of 'chemical clock' tracing the evolution massive star-forming regions. In this interpretation the methanol masers trace the most recently evaporated material, while the OH masers are found in more chemically evolved gas. Therefore, we would expect close association between the two maser species, but co-propagation would be rarer.

The last example is Harvey-Smith and Cohen (2005). They observed OH masers at 4.7 GHz toward many star-forming regions and compared with 1.7 GHz ground-state data for spatial and velocity coincidence. They found that there are some overlaps, 4765 MHz masers have 1720 MHz counterparts in five out of six cases and 1665 MHz counterparts in three out of six cases, with two cases of compound 4765/1720/1665 co-incidence of Masheder et al. (1994). Therefore, from Harvey-Smith and Cohen (2005) results support the association of 4765 MHz masers with 1720 MHz masers down to the level of individual maser spots. The production of a strong 4765 MHz maser requires among other things a long path-length and allow velocity gradient (Pavlakis and Kylafis, 1996). The physical conditions that can produce coincident 4765 MHz and 1720 MHz masers are shown in Table 2.1. Nevertheless, there is one work was published by Dodson and Ellingsen (2002) that inverse case of Gray et al. (1992) model, they have surveyed southern 4765 MHz masers with 0.6-arcsec positional accuracy and reported that 4765 MHz masers are more strongly associated with OH 6035 MHz masers than 1720 MHz masers.

This work highlighted the difficulties in co-propagation studies due to the observation factors. These problems can be helped by using consistent phase-calibration sources.

According to these observation results, there are some possibilities might try and search the coincidence between 1612 MHz OH masers & 6668 MHz methanol masers, 1665 MHz OH masers & 6035 MHz OH masers and 4765 MHz OH masers & 6035 MHz OH masers.

2.3.2 Introduction of Maser Physics

Masers are the result of microwave amplification by stimulated emission of radiation. They arise naturally in space when interstellar molecular are forced to interact with systems at several different temperatures and are unable to achieve a Maxwell-Boltzmann distribution of energies. In some cases the level populations become inverted. Stimulated emission which is the inverse of absorption, can then provide gain factors of up to 10^{10} in a single pass through the excited region of molecular gas. The powerful beams of molecular line radiation that emerge from compact maser sources are an astronishing spectacle of nature. The following sections introduce some of the main physical processes which are summarized from the review by Cohen (1989).

2.3.2.1 Radiative Transfer

Brightness or intensity (I_ν) is the energy per second per unit bandwidth per unit solid angle crossing unit area in the normal direction $\hat{n}$. We measure I_ν in units of W m^{-2} Hz^{-1} sr^{-1} or in terms of the brightness temperature (K) of an equivalent blackbody.

We define the specific emissivity, ϵ_ν W m^{-3} Hz^{-1} sr^{-1}, as the energy emitted per second per unit bandwidth per volume of the medium into unit solid angle. Thus the energy emitted into a cone of solid angle $d\Omega$ in time dt is

$$dE = \epsilon_\nu dV d\Omega d\nu dt, \tag{2.42}$$

We define the absorption co-efficient κ_ν m^{-1} as the fractional intensity absorbed from an incident beam per unit distance traveled;

$$dI_\nu = -\kappa_\nu I_\nu dS, \tag{2.43}$$

Hence for a beam of intensity I_ν and solid angle $d\Omega$ passing through a cylinder of length dS and cross section dA, the energy absorbed in time dt is

$$dE = \kappa_\nu I_\nu dA dS d\nu d\Omega dt, \tag{2.44}$$

The interaction between radio waves and neutral gas in the interstellar medium is governed by the radiative transfer

$$\frac{dI_\nu}{dS} = -\kappa_\nu I_{mu} + \epsilon_\nu, \tag{2.45}$$

where I_ν is the specific intensity of the radiation, ϵ_ν is the emissivity and κ_ν is the absorption coefficient of the gas. Consider for simplicity a two-level system. In this case the emissivity is

$$\epsilon_\nu = n_2 A_{21} \frac{h\nu_{21}}{4\pi} f(\nu), \tag{2.46}$$

where n_2 is the number density in the upper level, A_{21} is the Einstein coefficient giving the probability of spontaneous emission, ν_{21} is the mean frequency of the emitted photons and $f(\nu)$ is the normalised line profile and h is the Planck constant. The absorption coefficient is

$$\kappa_\nu = (n_1 B_{12} - n_2 B_{21} \frac{h\nu_{21}}{c} f(\nu), \tag{2.47}$$

where B_{12} is the Einstein coefficient for absorption and B_{21} is the coefficient for stimulated emission. The Einstein coefficients are related by the equations

$$A_{21} = B_{21} \frac{8h\nu^3}{\pi c^3}, \tag{2.48}$$

and

$$B_{12} = \frac{g_2}{g_1} B_{21}, \tag{2.49}$$

where g_i are the statistical weights of the upper and lower states.
The effect of stimulated emission is to reduce the absorption coefficient κ_ν. These are usually specified by an *excitation temperature* T_{ex} the temperature at which the populations would be in the Boltzmann ratio

$$\frac{n_2}{n_1} = \frac{g_2}{g_1}(-h\nu_{21}/kT_{ex}), \tag{2.50}$$

At radio frequencies $h\nu_{21}/k$ is of order 0.1 K, so for gas in local thermodynamic equilibrium the factor $h\nu_{21}/kT_{ex}$ is very small and stimulated emission almost cancels absorption. The net absorption coefficient is thus the difference between two much larger terms which are almost equal. As a result the radiative transfer through the gas is very sensitive to small changes in the level population shifts.

The solution to the equation of transfer is readily found to be

$$I_\nu = I_\nu(0) exp(-\tau_\nu) + \int_0^{\tau 0} \frac{j_\nu}{\kappa_\nu} exp\left[-(\tau_\nu - \tau_\nu')\right] d\tau_\nu', \tag{2.51}$$

where $I_\nu(0)$ is the intensity of radiation entering gas and τ_ν is the optical depth defined by $d\tau_\nu = \kappa_\nu dS$. Normally the optical depth would be a positive number, and the radiation reaching the observer would be the background radiation $I_\nu(0)$ attenuated by the factor $exp(-\tau_\nu)$, plus the emission (and absorption) from the cloud itself. For a maser, the absorption coefficient is negative, the optical depth is negative and so is the excitation temperature.

2.3.2.2 Saturation

There are limits to exponential growth, even in space. The radiation from cosmic masers usually grows to be so intense that stimulated emission begins to reduce the population inversion. The maser is then said to saturate, although, strictly speaking, only regions of the maser cloud are saturated.

The phenomenon of saturation has been treated analytically by Goldreich and Keeley (1972) for two simple cases: uniform spherical masers and cylindrical masers (long thin tubes). Their calculation is purely classical: each molecule is assumed to radiate at a precise frequency independently of the presence of other molecules and the strength of the radiation field. Then the level populations of a two-state maser are governed by the rate equations

$$\frac{\mathrm{d}n_2}{\mathrm{d}t} = -n_2 A_{21} - (n_2 - n_1)B_{21}J + P_2(n - n_1 - n_2) - \Gamma_2 n_2, \tag{2.52}$$

and

$$\frac{\mathrm{d}n_1}{\mathrm{d}t} = n_2 A_{21} + (n_2 - n_1)B_{21}J + P_1(n - n_1 - n_2) - \Gamma_1 n_1, \tag{2.53}$$

where n is the total density of the maser species, P_i is pump rate in to level i from all levels other then 1 and 2, Γ_i is the loss rate from level i and

$$J = \frac{1}{4\pi}\int\int I_{nu}\mathrm{d}\nu\mathrm{d}\Omega$$

is the number per maser photons crossing unit volume per second (from any direction). It has been assumed, without loss of generality, that the statistical weights of the maser states are equal. For steady state

$$(n_2 - n_1)(2B_{21}J + \Gamma_2) + 2n_2 A_{21} = (P_2 - P_1(n - n_1 - n_2) + n_1(\Gamma_1 - \Gamma_2), \tag{2.54}$$

The maser saturates wherever

$$J \sim \frac{\Gamma_2}{2B_{21}} = \frac{\Gamma_2}{A_{21}}\frac{4\pi\nu^3}{\pi c^3}, \tag{2.55}$$

The solutions of the rate equations are then substituted into the equation of radiative transfer, which is effectively one-dimensional in the cases considered by Goldreich and Keeley (1972).

2.3.2.3 Pumping

The theory of maser pumping is discussed extensively in the literature (e.g. Elitzur, 1982; Elitzur, 1992). In this thesis, we will discuss only the basic principles of pumping and outline some of the more recent works. In general, the system particles tend to populate the ground state. They are excited into higher levels by either collisions or radiation from an external source. The pumping scheme is

called *collisional* or *radiative* according to the nature of the process that dominates these excitations. The radiation produced internally in decays of excited states (the diffuse radiation) can never be considered the pumping agent: in the absence of external radiation or collision, all the system particles would cascade to the ground state and the diffuse radiation would disappear. But the diffuse radiation must always be taken into considerations because it can play an important role in shaping the population distribution among the system levels.

The study of potential pumping schemes requires construction of models that can adequately describe the population distribution of the system particles among the various energy levels. Thus, Cragg et al. (2002) discussed in detail modeling methanol and hydroxyl masers in star-forming regions by various pumping mechanisms. They concluded that in the model of Sobolev and Deguchi (1994)(hereafter the SD model), methanol molecules are excited to the second and first torsionally excited states by radiation from warm dust. Masers appear in certain *b*-type transitions, following the radiative and collisional cascade back to the ground state. The maser brightness and flux ratios are affected by beaming, and by the amplification of background photons from an underlying UCHII region, although neither of these features is essential for the creation of population inversions. The model can account for the extreme brightness of observed 6- and 12-GHz masers (Sobolev et al. 1997)(hereafter SCG97). The main line masers in OH can also be inverted by IR pumping. The IR transitions connect hyperfine multiplets of different rotational levels, so they occur in groups which are closely spaced in frequency. It has been known that line overlap can significantly influence the maser excitation in OH. Hence Cragg et al. (2002) extend the SD model by including line overlap, and apply the same model to both methanol and OH. Following a result of the OH masers which exhibited the pumping of 1665 MHz OH maser $^2\prod_{3/2}\, J = 3/2\ F = 1 - 1$, they found that this maser to be the dominant maser in their calculations so long as the affects of line overlap are included in the modeling. In the SD model 1665 MHz OH maser emission appears for gas temperatures $T_k < 125$ K under the conditions illustrated, with peak brightness $T_b \sim 10^{11}$ K. At low gas temperature ($T_k = 30$ K) the maser brightness is independent of density for $n_H < 10^8$ cm^{-3}(Figure 2.12), indicating that this maser is also radiative in origin and collisionally quenched. Bright masers require an OH specific column density in the range $10^{9.7} < N_{OH}/\Delta V < 10^{12.7}$cm^{-3} s and a hydrogen density $10^4 < n_H < 10^{8.3}$cm^{-3} for plausible values of the OH fractional abundance,$10^{-8.5} < X_{OH} < 10^{-5}$. At low gas temperature the maser is independent of dust temperature in the range examined (T_d=100 - 300 K), while at high gas temperature (T_k=150 K) the 1665 MHz maser is present only for high dust temperature $T_d > 200$ K or low gas densities $n_H < 10^7$ cm^{-3}.

2.3.3 Polarization and Stokes Parameter

2.3.3.1 Wave Polarization

From review of Kraus (1966), consider a plane wave traveling out of the page (positive z direction), as in Figure 2.13(a) with the electric field at all times in the y direction. This wave is said to be *linearly polarized*(in the y direction). As a

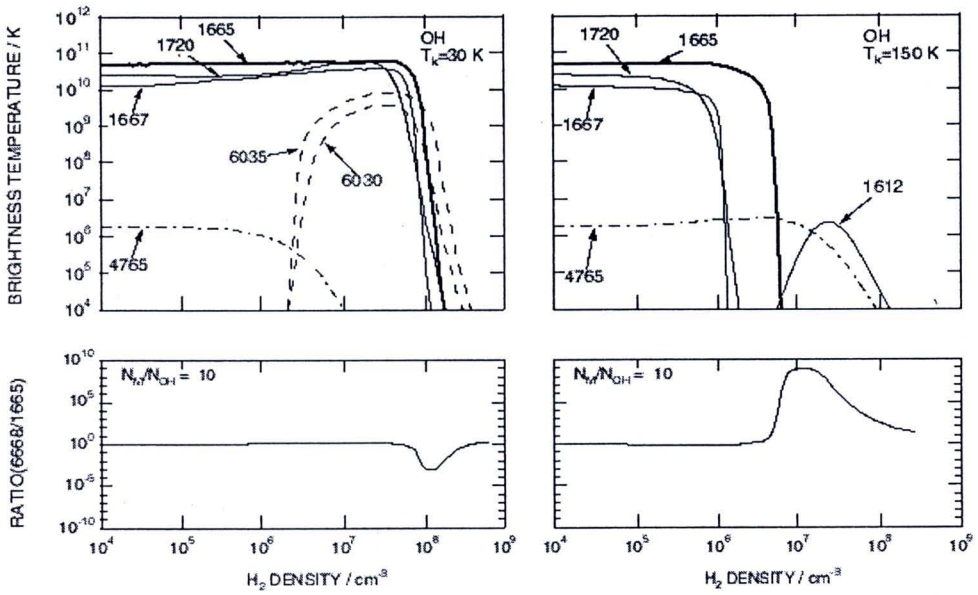

Figure 2.12 Brightness temperatures for selected masers of OH versus hydrogen density n_H, for $T_k = 30$ K (left-hand panels) and $T_k = 150$ K (right-hand panels). The remaining model parameters are fixed with values $T_d = 175$ K, $N_M/\Delta V = 10^{12.2}$ cm^{-3} s, $N_{OH}/\Delta V = 10^{11.2}$ cm $^{-3}$ s, $\epsilon^{-1} = 10$, and no UCHII background radiation. Botton panels show ratio of brightness temperatures for methanol 6668 MHz and OH 1665 MHz lines (taken from Cragg et al., 2002).

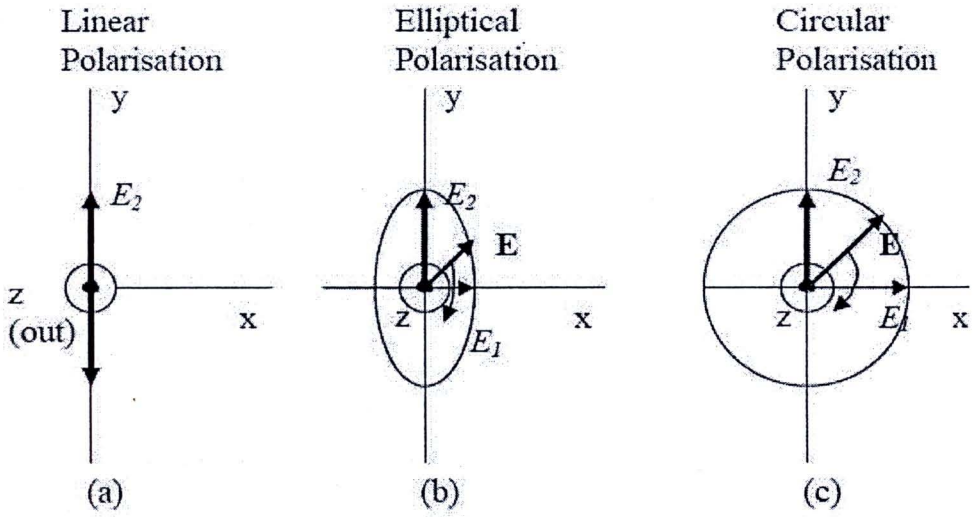

Figure 2.13 Relation of instantaneous electric field **E** to polarization ellipse.

function of time and position, the electric field is given by

$$E_y = E_2 \sin(\omega t - \beta z), \tag{2.56}$$

In general, the electric field vector of a wave traveling in the z direction may have both a y component and an x component, as suggested in Figure 2.13(b). In this more general situation, with a phase difference δ between the components, the wave is said to be *elliptically polarized.* At a fixed value of z the electrics vector **E** rotates as a function of time, that tip of the vector describing an ellipse called the *polarization ellipse.* The ratio of the major to minor axes of the polarization ellipse is called the *axial ratio* (AR). Thus, for the wave Figure 2.13(b), $AR = E_2/E_1$. Two extreme cases of elliptical polarization correspond to *circular polarization.* as in Figure 2.13(c), and *linear polarization*, as in Figure 2.13(a). For circular polarization $E_1 = E_2$ and $AR = 1$, while for linear polarization $E_1 = 0$ and $AR = \infty$.

In the most general case of elliptical polarization, the polarization ellipse may have any orientation, as suggested in Figure 2.14. The elliptically polarized wave may be expressed in terms of two linearly polarized components, one in the x direction and one in the y direction.

Thus, if the wave is traveling in the positive z direction (out of the page), the electric field components in the x and y directions are

$$E_x = E_1 \sin(\omega t - \beta z), \tag{2.57}$$

$$E_y = E_2 \sin(\omega t - \beta z + \delta), \tag{2.58}$$

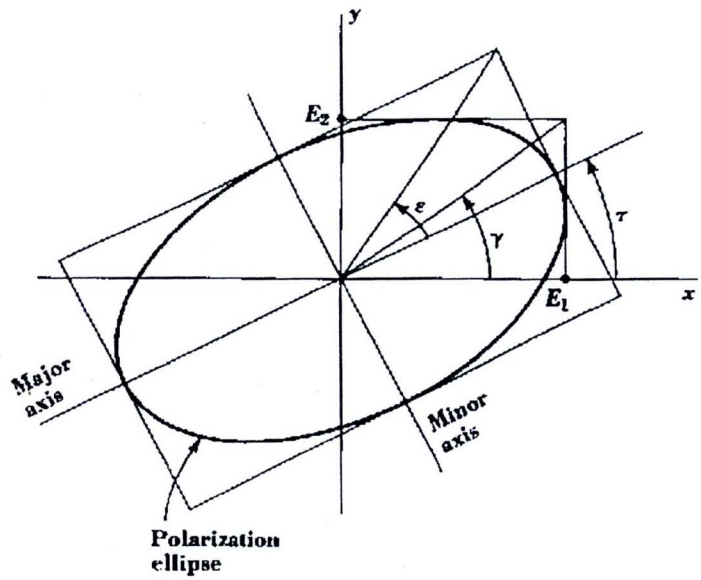

Figure 2.14 Polarization ellipse at tilt angle τ showing instantaneous components E_x and E_y and amplitudes (or peak values) E_1 and E_2.

where

E_1= amplitude of wave linearly polarized in x direction

E_2= amplitude of wave linearly polarized in y direction

δ= time-phase angle by which E_y leads E_x

Combining (2.57) and (2.58) gives the instantaneous total vector field $\mathbf{E}$:

$$\mathbf{E} = \hat{\mathbf{x}}E_1 \sin(\omega t - \beta z) + \hat{\mathbf{y}}E_2 \sin(\omega t - \beta z + \delta), \tag{2.59}$$

At $z = 0, E_x = E_1 \sim \omega t$ and $E_y = E_2 \sin(\omega t + \delta)$. Expanding E_y, yields

$$E_y = E_2(\sin \omega t \cos \sigma + \cos \omega t \sin \delta), \tag{2.60}$$

From the relation for E_x we have $\sin \omega t = E_x/E_1$ and $\cos \omega t = \sqrt{1 - (E_x/E_1)^2}$. Introducing these in (2.60) eliminates ωt, and, on rearranging, we obtain

$$\frac{E_x^2}{E_1^2} - \frac{2E_xE_y \cos \delta}{E_1E_2} + \frac{E_y^2}{E_2^2} = \sin^2 \delta, \tag{2.61}$$

or

$$aE_x^2 - bE_xE_y + cE_y^2 = 1, \tag{2.62}$$

where

$$a = \frac{1}{E_1^2 \sin^2 \delta},$$

$$b = \frac{2 \cos \delta}{E_1E_2 \sin^2 \delta},$$

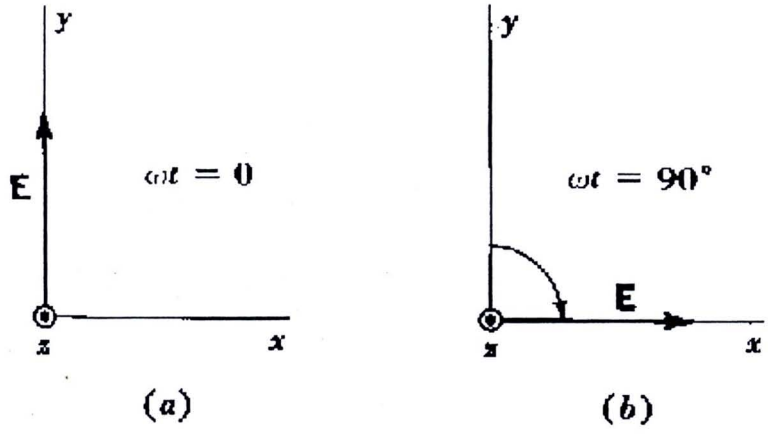

Figure 2.15 Change in direction of **E** for left circular polarization.

$$c = \frac{1}{E_2^2 \sin^2 \delta},$$

Equation $aE_x^2 - bE_xE_y + cE_y^2 = 1$ describes a (polarization) ellipse,as in Figure 2.14. The line segment OA is the semimajor axis, and the line segment OB is the semiminor axis. The tilt angle of the ellipse is τ. The axial ratio is,

$$AR = \frac{OA}{OB}, \tag{2.63}$$

when $(1 \leq AR \leq \infty)$.

If $E_1 = 0$, the wave is linearly polarized in the y direction. If E_2=0, the wave is linearly polarized in the x direction. If δ=0 and $E_1 = E_2$, the wave is linearly polarized but in a plane at an angle of 45° with respect to the x axis ($\tau = 45°$).

If $E_1 = E_2$ and $\delta = \pm 90°$, the wave is circularly polarized. When $\delta = +90°$, the wave is *left circularly polarized*, and when $\delta = -90°$, the wave is *right circularly polarized*.For the case $\delta = +90°$, at $z = 0$ and $t = 0$, that $E_x = 0$ and $E_y = E_2$, as in Figure 2.15-a. Under the same conditions but at a later time such that $\omega t = 90°$, $E_y = 0$ and $E_x = E_1$, as in Figure 2.15-b.

2.3.3.2 Partial Polarization and the Stokes Parameters

In general, the emission from celestial radio sources extends over a wide frequency range and within any finite bandwidth $\Delta\nu$ consists of the superposition of a large number of statistically independent waves of a variety of polarizations. The resultant wave is said to be randomly polarized. For such a wave we may write

$$E_x = E_1(t) \sin \omega t, \tag{2.64}$$

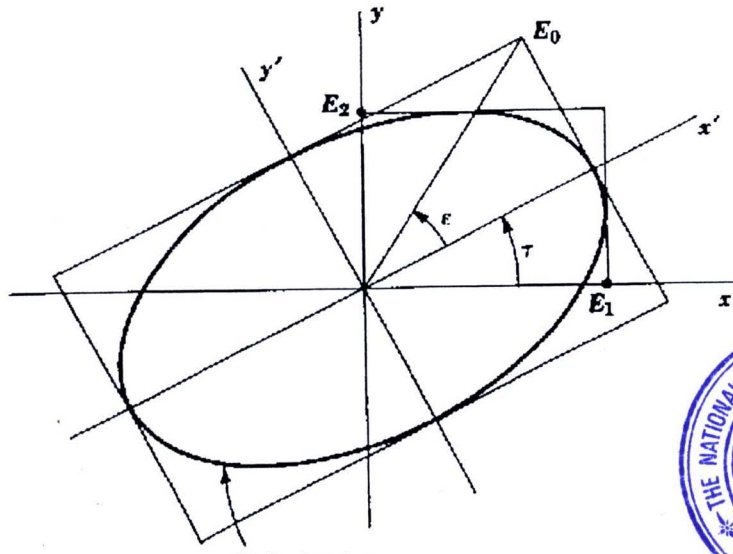

Figure 2.16 Relation of polarization-ellipse axes $(\acute{x}, \acute{y})$ to reference axes (x, y).

$$E_y = E_2(t)\sin[\omega t + \delta(t)], \tag{2.65}$$

where all the time functions are independent. The time variations of $E_1(t), E_2(t)$, and $\delta(t)$ are slow compared to that of the mean frequency, $\nu(\omega = 2\pi\nu)$ being of the order of the bandwith $\Delta\nu$.

To deal with partial polarization it is convenient to use the Stokes parameters introduced by Sir George Stokes (1852). As an introduction let us first consider their application to a completely polarized wave. Referring to Figure 2.16, we can write

$$E_x = E_1\sin(\omega t - \delta_1), \tag{2.66}$$

$$E_y = E_2\sin(\omega t - \delta_2), \tag{2.67}$$

where $\delta_1 - \delta_2 =$ phase difference of E_x and E_y.

The Stokes parameters I, Q, U, and V are defined as follows:

$$I = S = S_x + S_y = \frac{E_1^2}{Z} + \frac{E_2^2}{Z}, \tag{2.68}$$

$$Q = S_x - S_y = \frac{E_1^2}{Z} - \frac{E_2^2}{Z}, \tag{2.69}$$

$$U = S_x - S_y\tan 2\tau = 2\frac{E_1E_2}{Z}\cos(\delta_1 - \delta_2), \tag{2.70}$$

$$V = S_x - S_y \cot 2\tau = 2\frac{E_1 E_2}{Z} \sin(\delta_1 - \delta_2), \tag{2.71}$$

where S is the total poynting vector or flux density (watts per square meter) of the wave, Z is the intrinsic impedance of the medium (ohms per square)(Kraus, 1953). S_x represent the poynting vector for the wave component polarized in the x direction and S_y the poynting vector for the wave component polarized in the y direction.

2.3.4 The Spin of the Electron

What causes this splitting of the energy levels? A first step toward a solution was taken in 1924 by W. Pauli, who established that the doublet energy levels could be classified by a new quantum number j with the two values

$$j = l + \tfrac{1}{2} \text{ and } j = l - \tfrac{1}{2},$$

for the upper and lower levels of the doublet, respectively. (But in the exceptional case $l = 0$, the quantum number j has only a single value, $j = \frac{1}{2}$.) This new quantum number gives the magnitude of the total angular momentum **J** of the atom, according to the usual formula

$$|\mathbf{J}| = \sqrt{j(j+1)}\ \hbar, \tag{2.72}$$

But pauli offered no physics explanation of the difference between the orbital angular momentum (l) and total angular momentum (j). In 1925, S. Goudsmit and G. Uhlenbeck, who proposed that the electron is endowed with spin **s** , or *intrinsic angular momentum*, of magnitude

$$|\mathrm{s}| = \sqrt{\frac{3}{4}}\ \hbar, \tag{2.73}$$

or

$$|\mathrm{s}| = \sqrt{\frac{1}{2}(\frac{1}{2}+1)}\ \hbar, \tag{2.74}$$

Thus, the spin quantum number of the electron, the z - component of the spin is quantized in the usual way,

$$s_z = m_s \hbar = \pm\frac{1}{2}\ \hbar, \tag{2.75}$$

If $s_z = +\frac{1}{2}\hbar$, the electron is said to have spin *'up'*; if $s_z = -\frac{1}{2}\hbar$, spin *'down'*.

The energy difference between the $j = l + \frac{1}{2}$ level and the $j = l - \frac{1}{2}$ level in a doublet arises from the intrinsic magnetic moment of the electron. The theoretical analysis of the relativistic properties of quantum-mechanical particles confirms that an electron endowed with both spin and electron charge must necessarily have a magnetic moment. The magnetic moment is proportional to the spin,

$$\mu_e = -\frac{e}{m_e} s, \tag{2.76}$$

The minus sign in this equation indicates that the direction of the magnetic moment is opposite to the direction of the spin. The magnitude of the magnetic moment is

$$\mu_e = \frac{e\hbar}{m_e}\sqrt{\frac{3}{4}} = \frac{\sqrt{3}}{2}\frac{e\hbar}{m_e}, \tag{2.77}$$

or

$$\mu_{e,z} = -\frac{e}{m_e} m_s \hbar = \mp \frac{e}{m_e}\frac{\hbar}{2}, \tag{2.78}$$

The quantity $e\hbar/(2m_e)$ is called the **Bohr magneton.**

The magnetic moment μ_e placed in a magnetic field $\mathbf{B}$ has a potential energy

$$U = -\mu_e \cdot \mathbf{B} = \frac{e}{m_e}\mathbf{s} \cdot \mathbf{B}, \tag{2.79}$$

i.e., the potential energy is positive if $\mathbf{s}$ is parallel to $\mathbf{B}$ and negative if it is antiparallel.

The energy levels of most other atoms, with more than one electron, can be characterized by a similar set of quantum numbers. The net orbital angular momentum of the electrons of such an atom is the sum of the individual angular momenta of the electrons,

$$\mathbf{L} = \sum\nolimits_i \mathbf{L}_i, \tag{2.80}$$

Likewise, the net spin is

$$\mathbf{S} = \sum\nolimits_i \mathbf{s}_i, \tag{2.81}$$

and the total angular momentum is

$$\mathbf{J} = \mathbf{L}+\mathbf{S} = \sum\nolimits_i \mathbf{L}_i + \sum\nolimits_i \mathbf{s}_i, \tag{2.82}$$

all of these angular momenta obey the usual quantization rules. Thus

$$|\mathbf{L}| = \sqrt{L(L+1)}\,\hbar \tag{2.83}$$

$$|\mathbf{S}| = \sqrt{S(S+1)}\,\hbar, \tag{2.84}$$

and

$$|\mathbf{J}| = \sqrt{J(J+1)}\,\hbar, \tag{2.85}$$

2.3.5 The Zeeman Effect

The net magnetic moment of an atom with one or several electrons is the vector sum of all the magnetic moments associated with the spins plus all the magnetic moments associated with the orbital motion. By appealing once more to the Bohr model, we can understand how the orbital motion of an electron generates a magnetic moment. Imagine an electron of speed v in a circular orbit of radius r. The moving electron is equivalent to a circular current loop with current

$$I = \frac{(charge)}{(time)} = \frac{e}{2\pi r/v} = \frac{ev}{2\pi r}, \tag{2.86}$$

The magnetic moment of such a current loop is

$$\mu = (area) \times (current) = \pi r^2 \frac{ev}{2\pi r} = \frac{evr}{2}, \tag{2.87}$$

We can rewrite this as

$$\mu_L = -\frac{e}{2m_e} L, \tag{2.88}$$

where $L = m_e v r$ is the orbital angular momentum of the electron. For the net magnetic moment of the atom is the vector sum of these orbital and spin contributions,

$$\mu = -\frac{e}{2m_e} L - \frac{e}{m_e} S \tag{2.89}$$

$$= -\frac{e}{2m_e}(L + 2S), \tag{2.90}$$

To find the magnitude $|\mu|$ of this net magnetic moment and the component μ_z along the z-axis, we need to take into account the angular orientation of L and of S. The calculation is somewhat messy, and we will merely state the final result for μ_z,

$$\mu_z = -g m_j \frac{e\hbar}{2m_e}, \tag{2.91}$$

where $m = J, J-1, ..., 1-J, -J$, and the factor g, called the **Landé g-factor**, is

$$g = 1 + \frac{J(J+1) + S(S+1) - L(L+1)}{2J(J+1)}, \tag{2.92}$$

If we immerse an atom in an external magnetic field, the interaction between the atomic magnetic moment and the magnetic field will shift and split the energy levels of the atom. The splitting of spectral lines by external magnetic field is called the **Zeeman effect**. The Zeeman effect is also a very useful tool in astronomy since in permits the detection of the magnetic fields on stars,star-forming regions, and on the sun.

We can calculate the energy level in a magnetic field from an equation,

$$U = -\vec{\mu} \cdot \mathbf{B} = -\mu_z B, \tag{2.93}$$

or,

$$U = g m_j \frac{e\hbar B}{2m_e}. \tag{2.94}$$

Note that this energy shift removes the degeneracy of states with different values of m_J (and equal values of the other quantum numbers): in the presence of a magnetic field, states with different values of m_J have different energies.

2.3.6 Zeeman Splitting in the OH Molecules

Compact OH maser sources show strong polarization - especially those associated with HII regions (Class I OH sources). A characteristic of sources is their strong (nearly 100%)circular polarization and weaker linear polarization.

When circular polarization was first detected, it was attributed to Zeeman splitting by magnetic fields of a few milligauss in the OH cloud (Davies, 1974). Shklovskii (1969) suggested that twin source components of opposite circular polarization might be produced by a rotating OH cloud in which the lines are split by a Zeeman effect.

Linear polarization can result from directional pumping by unpolarised radiation which produces irregularities in the Zeeman sublevel populations, even in the absence of significant magnetic fields (e.g. Perkins et al., 1966). The possibility of a Zeeman interpretation of the circular polarization from some OH maser sources has again found favor with some authors Coles and Welch (1968), Rydbeck et al. (1970), Gardner et al. (1970), Litvak (1971), and Zuckerman et al. 1972). Goldreich et al. (1973) have given a theoretical discussion of the role of Zeeman splitting in producing polarization in astrophysical masers.

In this section the normal Zeeman pattern of OH will be described for the various transitions which have been observed in OH maser sources. These include the $^2\Pi_{1/2}$, $J = 1/2$ state triplet, $J = 3/2$ and $5/2$ quartets and the $^2\Pi_{3/2}$, $J = 3/2$ and $5/2$ quartets.

Each of the Π ground electron states mentioned above is split into two states by Λ doubling, and these in turn are doubled by hyperfine splitting, resulting in four states for each value of J. In a magnetic field each of these states is further split into $2F+1$ magnetic energy sublevels separated from the original energy level by

$$\Delta W = h\Delta v = -\mu_n g_I \cdot \frac{M_F B}{2F(F+1)} \cdot [I(I+1) + F(F+1) - J(J+1)],$$

$$= -\mu_0 g_J \cdot \frac{M_F B}{2F(F+1)} \cdot [J(J+1) + F(F+1) - I(I+1)], \qquad (2.95)$$

where μ_n and μ_0 are the nuclear and Bohr magneton ($\mu_n = \mu_0/1836$)
$g_1 \sim g_J \sim 1$, are the Landé g-factors;
$\mu_0/h = 1.39967 MHzG^{-1}$;
J=quantum number for the angular momentum including rotation but excluding nuclear spin;
F=total angular momentum; I=nuclear spin; M_F=the magnetic quantum number giving the projection of on the direction of the magnetic field; it takes the values $F, F-1, ..., -F+1, F$;
B=the magnetic field strength.

The first term(interaction of the nuclear magnetic moment with the magnetic field) of the splitting is negligible compared with the second term(the interaction of the electron magnetic moment with the magnetic field).

The Zeeman splitting pattern expected for a particular OH emission line results from transitions between the magnetic sub-levels of the two states, the upper state (m_2) and the lower state (m_1). Due to the dipole selection rules, the only transitions allowed are $\Delta m_F = m_2 - m_1 = -1, 0$ and $+1$. The $\Delta m_F = 0$ transitions are called π components and the $\Delta m_F = \mp 1$ are called σ components. In the absence of magnetic fields, the magnetic sub-levels are degenerate and all

Table 2.2 Zeeman splitting of the $^2\prod_{3/2}$, $J = 3/2$ ground state of OH (σ components).

Transitions	Frequency (MHz)	Zeeman Splitting between	Velocity Splitting ($km\ s^{-1}\ mG^{-1}$)
$^2\prod_{3/2}$, $J = 3/2$:			
$F = 1 \rightarrow 1$	1665.4	$\sigma^+ \longleftrightarrow \sigma^-$	0.590
$F = 2 \rightarrow 2$	1667.3	$\sigma^+ \longleftrightarrow \sigma^-$	0.354
$F = 1 \rightarrow 2$	1612.2	$\sigma^{+1} \longleftrightarrow \sigma^{-1}$	0.114
$F = 2 \rightarrow 1$	1720.5	$\sigma^{+2} \longleftrightarrow \sigma^{-2}$	0.342
		$\sigma^{+3} \longleftrightarrow \sigma^{-3}$	0.570

the different $m_2 \rightarrow m_1$ transitions occur at the common unperturbed frequency ν_{21}. The magnetic field shifts the energies of the magnetic sub-levels, and the line frequencies become;

$$\nu(m_2, m_1) = \nu_{21} + \frac{\mu_0 B}{h}(g_2 m_2 - g_1 m_1) = \nu_{21} + \frac{\nu_0 B}{h}(g_2 \Delta m + m_1 \Delta g), \quad (2.96)$$

where

$$g = g_J \frac{F(F+1) + J(J+1) - I(I+1)}{2F(F+1)}, \quad (2.97)$$

and $\Delta g = g_2 - g_1$. For $^2\prod_{3/2}$ state, $J = 3/2, I = 1/2$ and the factor g_J is 0.935. When $\Delta g = 0$, as in the case of OH main lines (at 1665 and 1667 MHz), the frequency shifts depend only on Δm_F and are independent of the specific values of the magnetic quantum numbers. Only three Zeeman components are generated in this case, corresponding to $m_F = 0, \pm 1$. But in OH satellite lines (1612 and 1720 MHz), where $\Delta g \neq 0$, the frequency of each transition $m_2 \rightarrow m_1$ is shifted by a different amount, which depends on both m_1 and m_2, leading to nine Zeeman components. The resulting Zeeman patterns for the $^2\prod_{3/2}$ state are shown in Figure 2.7. When the field points towards the observer and parallel to the line-of-sight, the σ^+ components ($\Delta m_F = +1$) are right circularly polarized, and the σ^- components ($\Delta m_F = -1$) are left circularly polarized. There is no emission from π components parallel to the field lines. If the magnetic filed is perpendicular to the line-of-sight, the σ components are linearly polarized perpendicular to the field, and the π components are linearly polarized parallel to the field. The relative intensities of the various σ and π components in Figure 2.7 have been estimated by Davies (1974) using Table 10.1 of Townes et al. (1956). The amount of Zeeman splitting in the 1665, 1667 and 1720 MHz transitions is given in Table 2.2.